Ultrathin, transferred layers of thermally grown silicon dioxide as biofluid barriers for biointegrated flexible electronic systems

Hui Fang[a,b,1], Jianing Zhao[b,c,1], Ki Jun Yu[a,b,1], Enming Song[b,d,1], Amir Barati Farimani[c,2], Chia-Han Chiang[e], Xin Jin[f], Yeguang Xue[g,h], Dong Xu[a,b], Wenbo Du[i], Kyung Jin Seo[a,b], Yiding Zhong[a,b], Zijian Yang[a,b], Sang Min Won[a,b], Guanhua Fang[a,b], Seo Woo Choi[a,b], Santanu Chaudhuri[i], Yonggang Huang[g,h], Muhammad Ashraful Alam[f], Jonathan Viventi[e], N. R. Aluru[c], and John A. Rogers[a,b,3]

[a]Department of Materials Science and Engineering, University of Illinois at Urbana–Champaign, Urbana, IL 61801; [b]Frederick Seitz Materials Research Laboratory, University of Illinois at Urbana–Champaign, Urbana, IL 61801; [c]Department of Mechanical Science and Engineering, University of Illinois at Urbana–Champaign, Urbana, IL 61801; [d]Department of Materials Science, Fudan University, Shanghai 200433, People's Republic of China; [e]Department of Biomedical Engineering, Duke University, Durham, NC 27708; [f]School of Electrical and Computer Engineering, Purdue University, West Lafayette, IN 47907; [g]Department of Mechanical Engineering, Northwestern University, Evanston, IL 60208; [h]Department of Civil and Environmental Engineering, Northwestern University, Evanston, IL 60208; and [i]Illinois Applied Research Institute, Urbana, IL 61820

Edited by Joseph M. DeSimone, University of North Carolina at Chapel Hill and Carbon, Chapel Hill, NC, and approved August 29, 2016 (received for review June 15, 2016)

Materials that can serve as long-lived barriers to biofluids are essential to the development of any type of chronic electronic implant. Devices such as cardiac pacemakers and cochlear implants use bulk metal or ceramic packages as hermetic enclosures for the electronics. Emerging classes of flexible, biointegrated electronic systems demand similar levels of isolation from biofluids but with thin, compliant films that can simultaneously serve as biointerfaces for sensing and/or actuation while in contact with the soft, curved, and moving surfaces of target organs. This paper introduces a solution to this materials challenge that combines (*i*) ultrathin, pristine layers of silicon dioxide (SiO_2) thermally grown on device-grade silicon wafers, and (*ii*) processing schemes that allow integration of these materials onto flexible electronic platforms. Accelerated lifetime tests suggest robust barrier characteristics on timescales that approach 70 y, in layers that are sufficiently thin (less than 1 μm) to avoid significant compromises in mechanical flexibility or in electrical interface fidelity. Detailed studies of temperature- and thickness-dependent electrical and physical properties reveal the key characteristics. Molecular simulations highlight essential aspects of the chemistry that governs interactions between the SiO_2 and surrounding water. Examples of use with passive and active components in high-performance flexible electronic devices suggest broad utility in advanced chronic implants.

thin-film encapsulation | thermal silicon dioxide | transfer printing | reactive molecular simulation | chronic implant

Advanced concepts in materials science and engineering form the foundations for emerging classes of high-performance, flexible electronic/optoelectronic devices, with levels of functionality that far exceed those of passive components and arrays. These systems are of interest because they can conform to the surfaces of biological systems in ways that enable important capabilities of relevance to both biomedical research and clinical practice. Examples include devices for continuous monitoring of health status through the skin (1–9), optical stimulation of targeted neural circuits in the brain (10–13), and electrophysiological mapping on the epicardial surface (14–17). These platforms are unique because their lightweight construction, thin geometry, and low bending stiffness allow high-quality, minimally invasive interfaces to soft, dynamic biological tissues, in a manner that cannot be replicated with conventional wafer-based forms of electronics. Such physical properties and mechanical attributes follow from the successful codevelopment of organic, inorganic, and hybrid inorganic/organic semiconductor materials together with mechanical designs and manufacturing schemes that enable their deployment in systems that can bend to small radii of curvature and, in some cases, stretch to high levels of elongation (2, 18–22). Skin-mounted devices, sometimes referred to as "epidermal" electronics (1), represent one of the most successful forms of this technology, where commercial embodiments are just now becoming widely available. Extensions of these types of systems for use as chronic implants have the potential to improve capabilities in human health care across broad categories of disease states and disorders (23, 24). A daunting challenge is in the development of materials that can serve as long-lived, perfect barriers to biofluids at thicknesses that allow high-quality sensing/actuating interfaces to the surrounding biology without adversely affecting the compliant mechanics.

In an ideal scenario, this material would encapsulate the entire front and back surfaces of the electronics, to prevent biofluid penetration across any exposed interfaces, with the following additional characteristics: (*i*) biocompatible molecular composition;

Significance

A critical obstacle of flexible electronics for chronic implants is the absence of thin-film barriers to biofluids with multidecade lifetimes. Previously explored materials are unsuitable due to limitations of (*i*) extrinsic factors, such as the practical inability to avoid localized defects, and/or (*ii*) intrinsic properties, such as finite water permeability. The work presented here overcomes these challenges by combining pristine thermal SiO_2 layers with processing steps for their integration onto flexible electronics. Experimental and theoretical studies reveal the key aspects of this material system. Accelerated immersion tests and cyclic bending measurements suggest robust, defect-free operation with various electronic components and an integrated system for multiplexed mapping of electrophysiological signals. The findings have broad relevance to diverse biointegrated electronics and optoelectronics.

Author contributions: H.F., J.Z., K.J.Y., E.S., and J.A.R. designed the research; H.F., J.Z., K.J.Y., E.S., A.B.F., C.-H.C., X.J., Y.X., D.X., K.J.S., Y.Z., Z.Y., S.M.W., G.F., S.W.C., Y.H., M.A.A., N.R.A., and J.A.R. performed the research; H.F., J.Z., K.J.Y., C.-H.C., W.D., S.C., J.V., and J.A.R. analyzed the data; and H.F., J.Z., K.J.Y., A.B.F., N.R.A., and J.A.R. wrote the paper.

The authors declare no conflict of interest.

This article is a PNAS Direct Submission.

[1]H.F., J.Z., K.J.Y., and E.S. contributed equally to this work.

[2]Present address: Department of Chemistry, Stanford University, Stanford, CA 94305.

[3]To whom correspondence should be addressed. Email: jrogers@illinois.edu.

This article contains supporting information online at www.pnas.org/lookup/suppl/doi:10.1073/pnas.1605269113/-/DCSupplemental.

(*ii*) high electrical capacitance (for electrical interfaces); (*iii*) low thermal conductivity and thermal mass (for thermal interfaces); (*iv*) good optical transparency (for optical interfaces); (*v*) low areal mass density (for minimized inertial load); (*vi*) low flexural rigidity (for conformal integration onto curved surfaces); (*vii*) defect-free, material perfection over large areas (several or many square centimeters); (*viii*) thermal and chemical compatibility with polymer substrates (for device fabrication) and (*ix*) lifetimes of multiple decades in electrolyte solutions at physiological pH and temperature, under cyclic bending conditions (for robust operation throughout the life of the patient). Despite more than a decade of research on this topic in academic and industrial groups around the world, there is currently no proven material system that offers these properties.

Established encapsulation schemes for conventional electronic implants such as pacemakers, cochlear implants, and deep-brain stimulators, rely on thick (millimeter-scale), rigid enclosures constructed using bulk metal or ceramic parts, incompatible with the types of flexible platforms discussed here (23, 25–27). Strategies based on thin flexible films are suitable for passive arrays of sensing/actuating electrodes or related devices (28–32), but they are not immediately applicable to active, semiconductor-based electronic platforms where continuous, or nearly continuous, applied voltages and induced currents are essential for operation (14, 18, 33–35). Organic/inorganic multilayer encapsulation schemes designed to protect flexible consumer electronic devices from oxygen and moisture have some promise (36–38), but known adaptations of them cannot address the extremely demanding conditions encountered in the body, where full immersion in warm, circulating biofluids on multidecade timescales is required.

Here, we report a different approach, based on an unusual materials solution that offers all of the nine attributes listed above. The scheme combines (*i*) defect-free, ultrathin layers of SiO_2 grown at high temperatures on the pristine, single crystalline surfaces of device-grade silicon wafers, with (*ii*) procedures for integrating these layers as uniform, front-side biofluid barriers and biointerfaces on flexible electronic platforms, and as backside barriers on their thin polymer supports. Detailed studies and comparative measurements against many of the most widely explored thin-film encapsulation strategies illustrate the exceptional characteristics that are possible. Thicknesses can range between tens and thousands of nanometers, in robust flexible geometries that are compatible with all important classes of materials and devices for flexible electronics. A combination of temperature-dependent measurements, microscopy investigations, electrical leakage and permeation tests, electrochemical impedance spectroscopic characteristics, and molecular dynamics simulations reveal the essential materials properties. Experiments with basic components, ranging from passive elements such as resistors, capacitors, and diodes to active, metal-oxide semiconductor transistors and multiplexed arrays, demonstrate compatibility with the highest performance types of flexible electronic devices.

Results

Thermal Growth of Ultrathin Layers of SiO_2 and Their Integration onto Flexible Plastic Substrates. Fig. 1*A* shows the four main steps for thermally growing, transferring, and integrating ultrathin layers of SiO_2 onto flexible electronic platforms. The process begins with thermal oxidation of a silicon wafer at ~1,100 °C. Standard semiconductor processing techniques and/or more recent methods in growth and transfer printing, enable fabrication of high-quality electronics on this layer of oxide, which for the illustrative example here consists simply of a pattern of gold (Au). The transfer consists of bonding the top surface of this substrate onto a thin polymer film (polyimide, 25 μm thick) on a glass substrate as a temporary, rigid support to facilitate manual manipulation. A combination of dry etching steps removes the silicon in a way

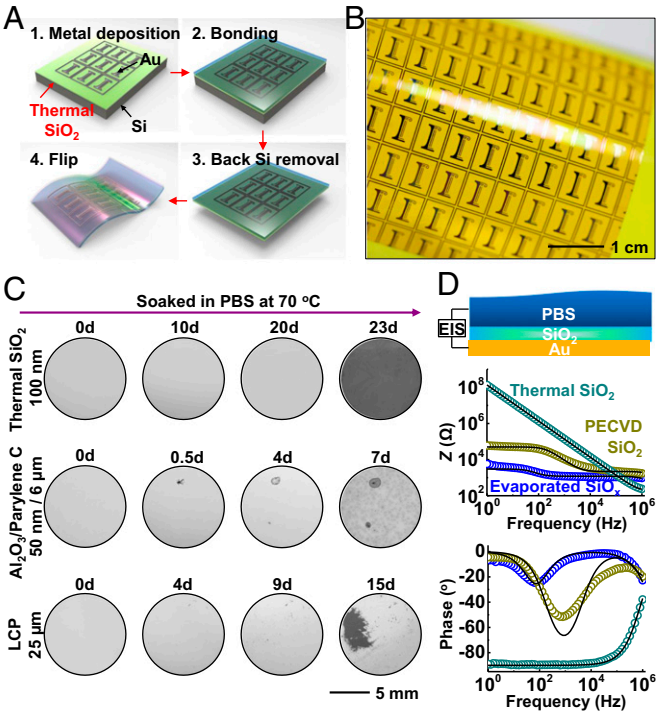

Fig. 1. Materials and integration strategies for use of ultrathin layers of SiO_2 thermally grown on device-grade silicon wafers, as water barriers in flexible electronics. (*A*) Schematic illustration of schemes for exploiting layers of thermal SiO_2 for encapsulation in test structures: (1) electron beam evaporation, photolithography, and etching of Mg to form "I"-shape patterns as test structures on SiO_2 thermally grown on a silicon wafer; (2) pressure bonding the top surface to a glass substrate that supports a thin film of polyimide (Kapton; 25 μm); (3) removal of the silicon wafer from back side by dry etching; (4) release of the final flexible test structure from the glass substrate. (*B*) Optical image of a sample produced in this manner, with a ~100-nm-thick layer of thermal SiO_2 on its top surface. (*C*) Sequential images of Mg encapsulated by layers of thermal SiO_2 and Al_2O_3/Parylene C and a bulk film of liquid crystal polymer (LCP) soaked in PBS solution at 70 °C. (*D*) EIS and modeling results for layers of SiO_2 grown by thermal oxidation and deposited by PECVD and electron beam evaporation.

that terminates at the bottom surface of the SiO_2 (*Materials and Methods*). Peeling the device from the temporary support completes the process, to yield a piece of flexible electronics encapsulated across its entire front surface with a layer of thermal SiO_2 as a defect-free barrier to biofluids, with chronic stability. Unlike traditional processing flows in which deposition of barrier layers occurs last, the scheme reported here starts with a planar, fully formed barrier and then builds device functionality directly on top. Similar growth and transfer processes can deliver a layer of SiO_2 to the bottom of the flexible substrate to prevent biofluid penetration from the back side. Details appear in *Materials and Methods*. Fig. 1*B* displays an image of a test vehicle that incorporates a front-side layer of SiO_2 with thickness of 100 nm (*SI Appendix*, Fig. S1). These steps can be easily scaled to the largest silicon wafers currently available (450-mm diameter), thereby allowing for systems with overall sizes that can provide nearly full area coverage across any internal organ of the human body. As in semiconductor manufacturing, the cost per unit area will decrease with increasing wafer sizes. In matured manufacturing processes, the costs for implementing these barrier coatings on biomedical implants have the potential to approach costs that are only incrementally larger than those of the wafers themselves.

A thin, uniform layer of magnesium (Mg) (200 nm thick, ~1-cm^2 area) formed by electron beam evaporation serves as a convenient

test vehicle for examining the water barrier properties of thin layers of SiO_2 grown and processed in this manner. Here, the strong reactivity of Mg with water [$Mg + 2H_2O \rightarrow Mg(OH)_2 + H_2$] quickly produces defects that can be visualized easily by standard microscopy techniques. As shown in Fig. 1*C* and *SI Appendix*, Tables S1 and S2, a 100-nm-thick layer of thermal SiO_2 survives for 22 d of complete, continuous immersion in phosphate-buffered saline (PBS) solution at pH of 7.4 and a temperature of 70 °C. After this period, the Mg layer dissolves at once, in a spatially uniform fashion across the entire area of the sample. Experiments performed in the same manner but with other candidate barrier materials, including various chemistries, deposition methods, thicknesses, and single/multilayer configurations, provide points of comparison. The results for all cases examined here indicate rapid degradation of the Mg in modes that involve either permeation directly through the barrier materials themselves (e.g., polymers deposited by spin coating), or through isolated, "pinhole" defects in the layers [e.g., silicon nitrides formed by plasma-enhanced chemical vapor deposition (PECVD)]. Specific examples of these intrinsic (former case) and extrinsic (latter case) effects appear in Fig. 1*C*. The only system, other than thermal SiO_2, that shows stable operation is a stainless-steel foil with thickness of 50 μm (*SI Appendix*, Fig. S2). This option is, however, not suitable for capacitive, biosensing applications, and it has only limited value in other possible biointerface measurements, such as those based on thermal or optical interfaces. Barrier layers formed by other deposition techniques, such as plasma-assisted atomic layer deposition (ALD), O_3-assisted ALD, and anodization show pinhole-like defects as well (39–42). For example, although plasma-assisted ALD-deposited SiN_x has a low intrinsic water vapor transmission rate, pinholes lead to extrinsic effects that limit the encapsulation performance of the entire barrier (40). The extent and nature of these types of extrinsic effects are expected to vary depending on the deposition methods, the deposition tools, and the detailed conditions for deposition and postprocessing, but they are unlikely to reach, on a consistent basis, the completely defect-free levels needed for the uses envisioned here. We note that additional areas of potential application of thermal SiO_2 barriers are in aseptic packaging, food containers, and others. Here, the performance of thermal SiO_2 thin-film barriers surpasses that of polymer-based antimicrobial food packaging layers by many orders of magnitude. Compared with some of the most advanced multilayer systems, such as the Barix barrier (developed by Vitex Systems, Inc.), thermal SiO_2 offers much lower water vapor transmission rates, even at thicknesses that are orders of magnitude smaller (37).

Electrochemical impedance spectroscopy (EIS) analysis of layers of SiO_2 formed by thermal growth and comparisons to those formed by other methods yield additional insights. One can interpret the EIS measurement by the equivalent circuit shown in *SI Appendix*, Fig. S3*A*. A pinhole-free ideal oxide in contact with the PBS solution can be represented by the solution resistance (R_{sol}) in series with the oxide capacitance (C_{ox}). In practice, the presence of pinholes provides a parasitic branch that contains the resistance of the solution within the pore (R_{po}), in series with a parallel combination of charge transfer resistance (R_{CT}) and double-layer capacitance (C_{dl}).

Fig. 1*D* presents results obtained in PBS solution. In direct contrast to electron beam evaporated SiO_x and PECVD SiO_2, thermal SiO_2 exhibits a nearly perfect capacitive response: in the log–log impedance vs. frequency figure (Fig. 1*D*, *Middle*), a plot of the impedance (Z) as a function of the frequency (f) exhibits a slope of −1. The results indicate that the oxide defines the total impedance, and that the signal is not corrupted by resistive leakage through pinholes/pores or by direct permeation. The plot in the bottom part of Fig. 1*D*, *Bottom*, shows that the phase remains fixed at −90° for frequencies up to 10^4 Hz

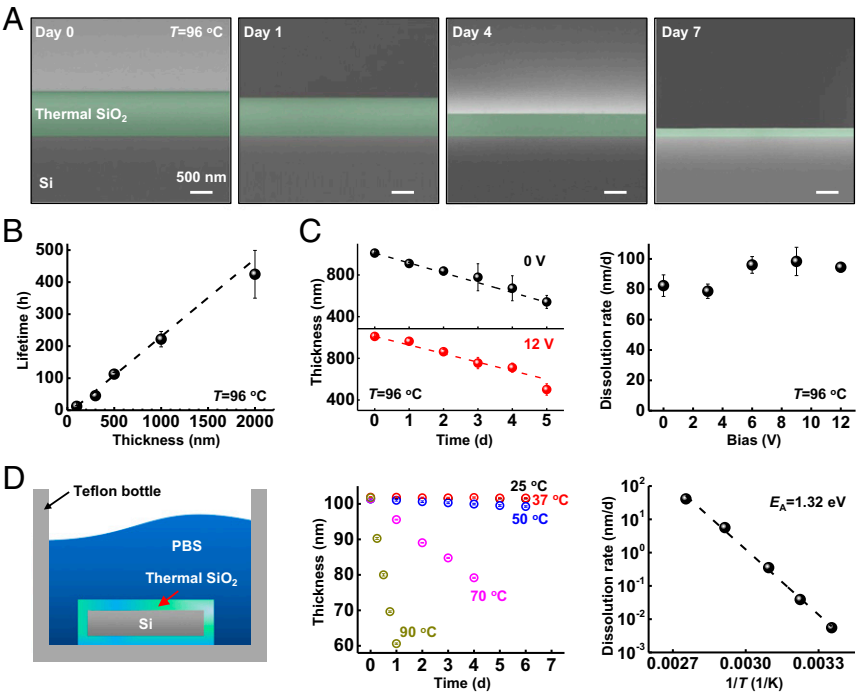

Fig. 2. Failure mechanisms associated with thermal SiO_2 encapsulation layers. (*A*) SEM images showing decreases in the thickness of a 1,000-nm-thick layer of thermal SiO_2 as a result of soaking in PBS at 96 °C. (*B*) Time before the leakage current reaches more than 100 nA, for thermal SiO_2 measured in an electrical leakage test (described in *SI Appendix*, Fig. S4). (*C*) Thickness changes associated with a 1,000-nm-thick layer of thermal SiO_2 without DC bias and with 12-V bias (*Left*), and extracted dissolution rate for voltages of 0, 3, 6, 9, and 12 V (*Right*). (*D*) Thermal SiO_2 on the surfaces and edges of a piece of Si in PBS solution (*Left*) allowed measurements of changes in thickness at different temperatures (*Center*). The results indicate a linear relationship between the dissolution rate and 1/*T* (*Right*).

(capacitive response of a *R–C* series circuits), as further support of this conclusion. The phase rises to −40° at 10^6 Hz as the solution resistance begins to contribute to the response. The oxide capacitance extracted from the plot (~1 nF) is consistent with the known thickness and dielectric constant. Because $C_{dl} \gg C_{ox}$, this parameter does not affect the measurements of thermal SiO_2 (*SI Appendix*, Fig. S3).

Chemical and Physical Effects in Electrical Leakage Through Layers of SiO_2. Results of electrical leakage tests (see *SI Appendix* for experimental details) conducted using thermal SiO_2 at thicknesses of 100, 300, 500, 1,000, and 2,000 nm at 96 °C to accelerate failure-related chemical/physical processes appear in Fig. 2*A* and *SI Appendix*, Fig. S4, with comparison with conventional inorganic and organic materials (*SI Appendix*, Figs. S4 and S5). The results show abrupt transitions to high leakage currents at time durations that depend linearly on the thickness. Fig. 2*A* displays colorized cross-sectional scanning electron microscope (SEM) images of a 1,000-nm-thick layer at various times after immersion. The results indicate a systematic reduction in the thickness, likely due to dissolution by hydrolysis, $SiO_2 + 2H_2O \rightarrow Si(OH)_4$ (*SI Appendix*, Fig. S6; dissolution occurs also for stainless steel as summarized in *SI Appendix*, Fig. S7). The timescale for complete dissolution is consistent with that for the appearance of large leakage currents, as shown in Fig. 2*B*, which illustrates the linear dependence of lifetime (i.e., time to large leakage current) on thickness. This linear form, and its zero intercept, also suggests that hydrolysis proceeds exclusively by surface reactions without a significant role of reactive diffusion into the bulk of the SiO_2 or of permeation through defect sites. Additional studies show that the dissolution rate for thermal SiO_2 does not depend on electrical bias for values relevant to biointegrated electronics (Fig. 2*C*).

Temperature-dependent studies of the rate of hydrolysis of thermal SiO_2 in PBS reveal additional details. These experiments use thermal SiO_2 grown on all surfaces of the silicon wafer, including its edges (Fig. 2*D*), to avoid any exposed Si, which itself will dissolve according to $Si + 4H_2O \rightarrow Si(OH)_4 + 2H_2$ (*SI Appendix*, Fig. S8). The dissolution rates depend exponentially on $1/T$, consistent with Arrhenius scaling and an apparent activation energy $E_A = 1.32$ eV (Fig. 2*D*). This energy is higher than that inferred from previous studies of natural quartz mineral and fused amorphous silica (0.48–1.11 eV) in deionized water or various aqueous solutions (such as NaCl solution), possibly due to the formation of activated complexes on the surfaces of SiO_2 in PBS (43, 44). For comparison, measurement of the dissolution rate at a pH of 7.4 and 70 °C yields a value of 5.6 nm/d (2.9×10^{-13} mol/cm^2·s), which is roughly one order of magnitude higher than that of quartz or amorphous silica in deionized water at the same temperature (44, 45). This increase is likely due to an expected "salt effect" that leads to enhanced reaction rates in PBS (46). From these measurements, a multiphysics computational model for the temperature and pH dependence of the dissolution rate has been developed and validated (*Materials and Methods*). The dissolution rate is found to have a half-order dependence on hydroxide concentration (*SI Appendix*, Fig. S9). Simulations can yield estimates of the lifetime of thermal SiO_2 layers for pH values ranging from 7 to 12, and temperatures from 25 to 90 °C. At a pH of 7.4 and 37 °C, the dissolution rate for thermal SiO_2 is $\sim 4 \times 10^{-2}$ nm/d, corresponding to a lifetime of nearly 70 y. This timescale exceeds the lifetime of most patients who might benefit from chronic flexible electronic implants, for a layer with thickness of 1,000 nm, sufficiently thin to meet the key requirements outlined previously.

Theoretical Modeling. Reactive molecular dynamics (RMD) simulations (Fig. 3 *A* and *B*) provide some additional insights into the dissolution chemistry. Fig. 3*A* presents schematic illustrations of the simulation box explained in detail in *Materials and Methods*.

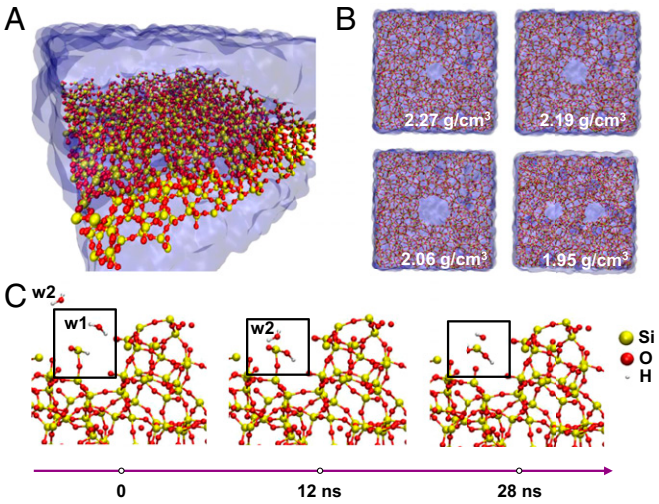

Fig. 3. Reactive molecular dynamics (RMD) simulations of hydrolysis of defective layers of SiO_2. (*A*) Perspective snapshot of the SiO_2 slab in water. (*B*) Top-view representation of four different oxide densities of the SiO_2 slab in water. (*C*) Simulation snapshots of hydrolysis reactions that lead to the dissociation of one molecule of SiO_2 from the structure.

Adding/removing protons from the system provides a means to adjust the pH of the surrounding bath that is free of ions. As shown in Fig. 3*B*, adding void-like defects in a perfect material serves as a route to reduce the effective density, motivated partly by previous work that shows that voids and defects larger than 1 nm can exist in SiO_2 structures (47, 48). Fig. 3*C* depicts snapshots of sequential reactions that lead to the dissociation of Si from a surface defective site, with a dangling Si–OH, or Si–H bond. On average, ~80% of the Si in the oxide layer are OH terminated and ~20% are H terminated. Analysis therefore focuses on the dissolution chemistry of the former. The frame on the left ($t = 0$ ns) shows two water molecules (labeled w1 and w2) that approach a Si atom at the location of a Si–OH bond. At $t = 12$ ns, the hydrogen of molecule w1 dissociates and forms a bond with the H from the –OH– terminated Si and yields H_2. This reaction increases the length of the bond between the Si and the O on the bottom side from 2.3 to 2.95 Å, with a corresponding reduction in its strength. At $t =$ 28 ns, molecule w2 approaches the Si and one of its hydrogen atoms dissociates in the vicinity of the dissolution site (Fig. 3*C*). This hydrogen chemically bonds with the dangling O of the Si. Cleavage of the previously weakened Si–O bond releases the ionic species $Si(OH)_2^{2+}$. The w2 remains as OH^- for an additional 3 ns and forms a water molecule by bonding with another H^+ at $t =$ 31 ns. The conversion of $Si(OH)_2^{2+} \rightarrow Si(OH)_4$ finishes at 80–90 ns at $T = 37$ °C, such that the final product of dissolution is silicic acid, similar to findings from previous studies of dissolution of bulk Si using comparable models (49). These reaction products appear within the 35-ns timescale of the simulations presented here under accelerated conditions, that is, at 100 °C, $Si(OH)_2^{2+} \rightarrow Si(OH)_3^+ \rightarrow Si(OH)_4$ occurs in ~32 ns (*SI Appendix*, Fig. S10). Simulation results of different mass density, influence of defects, and temperature dependence on intermediate products during Si hydrolysis are detailed in *SI Appendix* (*SI Appendix*, Figs. S11 and S12).

Water Barriers Demonstrated in Key Electronic Devices. The overall process outlined in Fig. 1*A* provides versatility for application with nearly any class of silicon or silicon-compatible electronic systems, and with other forms of flexible electronics. Resistors, capacitors, p-n diodes, and metal–oxide–semiconductor field effect transistors (MOSFETs) based on silicon nanomembranes serve as examples, each constructed with a 1-μm-thick layer of

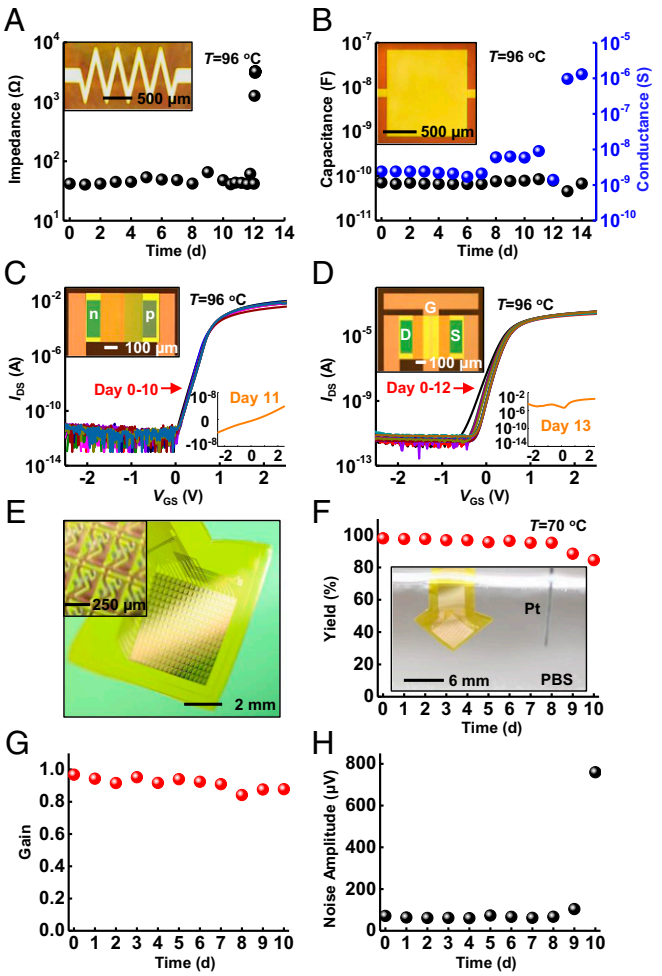

Fig. 4. Demonstration of electronic devices and flexible electronic systems encapsulated with thermal SiO_2. (*A–D*) Results of soak tests of resistors, capacitors, diodes, and *n*-type metal–oxide–semiconductor transistors with optical images (*Insets*). Tests in PBS solutions at 96 °C indicate that failure occurs at day 12 for all devices. (*E*) A photograph of a platform of active multiplexed flexible electronics with double-sided thermal SiO_2 encapsulation in a slightly bent configuration. The *Inset* presents a magnified view of the sensing sites, each of which consists of one sensing transistor and one multiplex transistor connected in series. (*F–H*) Accelerating soak test with in vitro measurement of electrical performance including yield (Y/Y_0, defined as the number of working sensing sites divided by the total number of sites), gain (the ideal gain is 1), and mean noise rms. The results indicate device stability throughout 9 d in 70 °C PBS. The *Inset* in *F* presents a photograph of an active multiplex device fully immersed in PBS.

thermal SiO_2 (Fig. 4 *A–D*, *SI Appendix*, Fig. S13, and tested in the manner illustrated in *SI Appendix*, Fig. S4, *Left*). All devices retain functionality, without measurable change from their initial state, during complete immersion in PBS at 96 °C (*SI Appendix*, Figs. S14 and S15). The SiO_2 fully dissolves in 12 ± 1 d, consistent with data presented previously. At this time, all devices fail suddenly and catastrophically. For example, the resistor behaves as an open circuit (Fig. 4*A*). For the capacitor, ions penetrate into the polyimide dielectric, which significantly increases the capacitance and contributes to leakage current across this layer (Fig. 4*B*). The characteristics of the diode and the *n*-channel MOSFET change to resemble those of a resistor, as illustrated in Fig. 4 *C* and *D*. As described previously, an additional transfer step can integrate a layer of thermal SiO_2 on the back side of the polyimide substrate, to prevent water penetration through this surface. *SI Appendix*, Fig. S16*A*, shows a sample with this type of design, in which a patterned layer of Mg persists unchanged for up to 15 d during complete immersion (without well structure) in PBS at 70 °C. Under similar conditions, samples without the thermal SiO_2 layer on the back side of the polyimide fail within a few hours due to water permeation directly through the polyimide (*SI Appendix*, Figs. S16 and S17). *SI Appendix*, Fig. S18, demonstrates applicable flexibility of this design with 5 mm of bending radius.

In addition to water, ions present in biofluids such as Na^+ and K^+ can also degrade/alter performance, particularly in active semiconductor devices. For example, proximity of Na^+ to the conducting channel of a MOSFET causes its threshold voltage to shift. The challenge is that these and other ions have a non-negligible mobility inside the bulk of the thermal SiO_2 material. The transport is, in general, dependent on electric field, such that operation of the device can enhance this drift. When the ion transport is drift dominated, the failure time is proportional to the ion transition time $\tau_{trans} = h/\mu\xi = h^2/\mu V = kTh^2/DqV$, where h is the thickness of thermal SiO_2, μ is the mobility of the ion, ξ is the internal electric field, V is the voltage across the SiO_2, k is the Boltzmann constant, T is temperature, D is the diffusivity of the ion, and q is the charge. In practice, the lifetime increases significantly with reductions in voltages (for a fixed thickness) and/or increases in thickness (at fixed voltage). Self-consistent simulations described in *Materials and Methods* show that ions accumulate inside the thermal SiO_2 where they can change the potential distribution in a manner that alters the transport (*SI Appendix*, Figs. S19 and S20). Solutions to the coupled drift-diffusion and Poisson's equation for Na^+ indicate that devices last several times longer than expected based on purely drift-dominated transport (which provides the lower bound for device lifetime; *SI Appendix*, Fig. S21). Penetration of ions can be further retarded by the incorporation of high-quality silicon nitride or phosphosilicate glass, as adopted by the semiconductor industry since the 1980s (50, 51). An ideal barrier for both water and ions may come from thin layers of thermal nitride, oxide/nitride bilayers, or even oxynitrides. Exploration of these possibilities is a topic of current work.

Integration of 900-nm thermal SiO_2 as encapsulation for actively multiplexed electronics designed to allow high-speed spatiotemporal mapping of biopotentials highlights the compatibility of the materials and concepts introduced here with the most sophisticated classes of flexible electronics. Fig. 4*E* and *SI Appendix*, Fig. S22, present exploded view schematic illustrations of the system and an image of a completed device with top- and bottom-side thermal SiO_2 encapsulation, respectively. This platform provides 252 sensing sites (18 rows by 14 columns) with silicon transistors at each site for actively multiplexed addressing, over an area of 4.5 mm × 4.6 mm. The multiplexing is realized by connecting a pair of transistors in series, one of which functions for capacitive sensing of biopotentials through thermal SiO_2 by connecting its gate terminal to an electrode pad. The other transistor serves as a switch to allow multiplexed readout from the sensing site (*SI Appendix*, Figs. S23 and S24). In addition to its barrier role, the front-side SiO_2 layer acts as the dielectric layer for capacitive coupling. Fig. 4 *F–H* shows excellent yield, stable high average gain values with low noise operation during complete immersion in PBS solution at 70 °C for 10 d. *SI Appendix*, Fig. S25, illustrates robust performances in bending test. Although the approaches presented here do not encapsulate the exposed edges at the periphery of the overall device platforms, this constraint seems to have little practical effect on the lifetimes for the cases examined. One potential limitation is that SiO_2/polymer interface might suffer from delamination, especially under external stimuli such as thermal cycles (52). Ongoing efforts seek to eliminate edges entirely by use of slightly oversized layers of thermal SiO_2 together with SiO_2/SiO_2 bonding chemistries adapted from the semiconductor industry.

Conclusions

In summary, the results presented here establish materials strategies and integration schemes for use of ultrathin layers of SiO_2

thermally grown on device-grade Si wafers as long-lived water barriers for active, flexible electronic systems. Comparisons against conventional encapsulation strategies highlight the advantages. Detailed experimental and theoretical investigations reveal that a slow hydrolysis process defines the ultimate lifetimes, consistent with the exceptionally high quality of SiO_2 films formed and manipulated in the schemes introduced here. In regimes of thicknesses compatible with mechanically flexible form factors, and in layouts that can support high-quality electrical interfaces, accelerated testing and modeling at both atomistic and continuum length scales suggest robust operation over many decades at physiological temperatures. Results presented here used PBS as the test solution. Lifetimes in biofluids may be somewhat different, due to differences in composition. Demonstrations at wafer-level sizes and in dual-sided encapsulation geometries illustrate the scalability of these approaches to devices of relevance for nearly all envisioned applications in biointegrated electronics. It is important to acknowledge practical difficulties in application of the ideas presented here to systems with challenging topography such as those that involve arrays of penetrating pin-type electrodes. Future efforts include developing schemes to address such applications, exploring advanced embodiments that can inhibit both water and ion permeation, and implementing these concepts in electronic and optoelectronic devices for neural and cardiac applications.

Materials and Methods

Details of fabrication steps, device structures of Mg tests, impedance measurement, and electrical leakage tests are shown in *SI Appendix*. Theoretical analysis including EIS modeling, multiphysics simulations of thermal SiO_2 dissolution, molecular simulations, and sodium ion transport simulations also appear in *SI Appendix*.

ACKNOWLEDGMENTS. We acknowledge the Micro and Nanotechnology Laboratory for device fabrication and the Beckman Institute for Advanced Science and Technology for device measurement. This work was supported by Defense Advanced Research Projects Agency Contract HR0011-14-C-0102, National Science Foundation Award 1403582, National Science Foundation Award CCF-1422914, and Army Research Office Award W911NF-14-1-0173, and performed in the Frederick Seitz Materials Research Laboratory and the Center for Microanalysis of Materials at the University of Illinois at Urbana–Champaign. J.Z. acknowledges supports from Louis J. Larson Fellowship, Swiegert Fellowship, and H. C. Ting Fellowship from the University of Illinois at Urbana–Champaign. E.S. acknowledges support from China Scholarship Council.

1. Kim D-H, et al. (2011) Epidermal electronics. *Science* 333(6044):838–843.
2. Lipomi DJ, et al. (2011) Skin-like pressure and strain sensors based on transparent elastic films of carbon nanotubes. *Nat Nanotechnol* 6(12):788–792.
3. Xu S, et al. (2014) Soft microfluidic assemblies of sensors, circuits, and radios for the skin. *Science* 344(6179):70–74.
4. Gao W, et al. (2016) Fully integrated wearable sensor arrays for multiplexed in situ perspiration analysis. *Nature* 529(7587):509–514.
5. Wu W, et al. (2014) Piezoelectricity of single-atomic-layer MoS_2 for energy conversion and piezotronics. *Nature* 514(7523):470–474.
6. McAlpine MC, Ahmad H, Wang D, Heath JR (2007) Highly ordered nanowire arrays on plastic substrates for ultrasensitive flexible chemical sensors. *Nat Mater* 6(5):379–384.
7. Kaltenbrunner M, et al. (2013) An ultra-lightweight design for imperceptible plastic electronics. *Nature* 499(7459):458–463.
8. Lochner CM, Khan Y, Pierre A, Arias AC (2014) All-organic optoelectronic sensor for pulse oximetry. *Nat Commun* 5:5745.
9. Son D, et al. (2014) Multifunctional wearable devices for diagnosis and therapy of movement disorders. *Nat Nanotechnol* 9(5):397–404.
10. Jeong J-W, et al. (2015) Wireless optofluidic systems for programmable in vivo pharmacology and optogenetics. *Cell* 162(3):662–674.
11. Montgomery KL, et al. (2015) Wirelessly powered, fully internal optogenetics for brain, spinal and peripheral circuits in mice. *Nat Methods* 12(10):969–974.
12. Kim TI, et al. (2013) Injectable, cellular-scale optoelectronics with applications for wireless optogenetics. *Science* 340(6129):211–216.
13. Canales A, et al. (2015) Multifunctional fibers for simultaneous optical, electrical and chemical interrogation of neural circuits in vivo. *Nat Biotechnol* 33(3):277–284.
14. Viventi J, et al. (2010) A conformal, bio-interfaced class of silicon electronics for mapping cardiac electrophysiology. *Sci Transl Med* 2(24):24ra22.
15. Kim D-H, et al. (2011) Materials for multifunctional balloon catheters with capabilities in cardiac electrophysiological mapping and ablation therapy. *Nat Mater* 10(4):316–323.
16. Xu L, et al. (2014) 3D multifunctional integumentary membranes for spatiotemporal cardiac measurements and stimulation across the entire epicardium. *Nat Commun* 5:3329.
17. Kim D-H, et al. (2012) Electronic sensor and actuator webs for large-area complex geometry cardiac mapping and therapy. *Proc Natl Acad Sci USA* 109(49):19910–19915.
18. Sekitani T, Zschieschang U, Klauk H, Someya T (2010) Flexible organic transistors and circuits with extreme bending stability. *Nat Mater* 9(12):1015–1022.
19. Schwartz G, et al. (2013) Flexible polymer transistors with high pressure sensitivity for application in electronic skin and health monitoring. *Nat Commun* 4:1859.
20. Tian B, et al. (2010) Three-dimensional, flexible nanoscale field-effect transistors as localized bioprobes. *Science* 329(5993):830–834.
21. Wu W, Wen X, Wang ZL (2013) Taxel-addressable matrix of vertical-nanowire piezotronic transistors for active and adaptive tactile imaging. *Science* 340(6135):952–957.
22. Rogers JA, Someya T, Huang Y (2010) Materials and mechanics for stretchable electronics. *Science* 327(5973):1603–1607.
23. Wilson BS, et al. (1991) Better speech recognition with cochlear implants. *Nature* 352(6332):236–238.
24. Hochberg LR, et al. (2006) Neuronal ensemble control of prosthetic devices by a human with tetraplegia. *Nature* 442(7099):164–171.
25. Bowman L, Meindl JD (1986) The packaging of implantable integrated sensors. *IEEE Trans Biomed Eng* 33(2):248–255.
26. Sanders RS, Lee MT (1996) Implantable pacemakers. *Proc IEEE* 84(3):480–486.
27. Mayberg HS, et al. (2005) Deep brain stimulation for treatment-resistant depression. *Neuron* 45(5):651–660.
28. Rousche PJ, Normann RA (1998) Chronic recording capability of the Utah Intracortical Electrode Array in cat sensory cortex. *J Neurosci Methods* 82(1):1–15.
29. Harrison RR, et al. (2007) A low-power integrated circuit for a wireless 100-electrode neural recording system. *IEEE J Solid-State Circuits* 42(1):123–133.
30. Hoogerwerf AC, Wise KD (1994) A three-dimensional microelectrode array for chronic neural recording. *IEEE Trans Biomed Eng* 41(12):1136–1146.
31. Wise KD, Anderson DJ, Hetke JF, Kipke DR, Najafi K (2004) Wireless implantable microsystems: High-density electronic interfaces to the nervous system. *Proc IEEE* 92(1):76–97.
32. Tyler DJ, Durand DM (2002) Functionally selective peripheral nerve stimulation with a flat interface nerve electrode. *IEEE Trans Neural Syst Rehabil Eng* 10(4):294–303.
33. Viventi J, et al. (2011) Flexible, foldable, actively multiplexed, high-density electrode array for mapping brain activity in vivo. *Nat Neurosci* 14(12):1599–1605.
34. Khodagholy D, et al. (2013) In vivo recordings of brain activity using organic transistors. *Nat Commun* 4:1575.
35. Bellin DL, et al. (2014) Integrated circuit-based electrochemical sensor for spatially resolved detection of redox-active metabolites in biofilms. *Nat Commun* 5:3256.
36. Thejo Kalyani N, Dhoble SJ (2015) Novel materials for fabrication and encapsulation of OLEDs. *Renew Sustain Energy Rev* 44:319–347.
37. Park J-S, et al. (2011) Thin film encapsulation for flexible AM-OLED: A review. *Semicond Sci Technol* 26(3):034001.
38. Ahmad J, Bazaka K, Anderson LJ, White RD, Jacob MV (2013) Materials and methods for encapsulation of OPV: A review. *Renew Sustain Energy Rev* 27:104–117.
39. Xie X, Rieth L, Merugu S, Tathireddy P, Solzbacher F (2012) Plasma-assisted atomic layer deposition of Al_2O_3 and parylene C bi-layer encapsulation for chronic implantable electronics. *Appl Phys Lett* 101(9):93702.
40. Andringa A-M, et al. (2015) Low-temperature plasma-assisted atomic layer deposition of silicon nitride moisture permeation barrier layers. *ACS Appl Mater Interfaces* 7(40):22525–22532.
41. Huang Y, et al. (2008) Evaluation of the corrosion resistance of anodized aluminum 6061 using electrochemical impedance spectroscopy (EIS). *Corros Sci* 50(12):3569–3575.
42. Yong-Qiang Y, et al. (2014) High barrier properties of transparent thin-film encapsulations for top emission organic light-emitting diodes. *Org Electron* 15(6):1120–1125.
43. Worley WG (1994) Dissolution kinetics and mechanisms in quartz- and grainite-water systems. PhD dissertation (Massachusetts Institute of Technology, Cambridge, MA).
44. Knauss KG, Wolery TJ (1988) The dissolution kinetics of quartz as a function of pH and time at 70 °C. *Geochim Cosmochim Acta* 52(1):43–53.
45. Icenhower JP, Dove PM (2000) The dissolution kinetics of amorphous silica into sodium chloride solutions: Effects of temperature and ionic strength. *Geochim Cosmochim Acta* 64(24):4193–4203.
46. Dove PM, Han N, De Yoreo JJ (2005) Mechanisms of classical crystal growth theory explain quartz and silicate dissolution behavior. *Proc Natl Acad Sci USA* 102(43):15357–15362.
47. Gibson JM, Dong DW (1980) Direct evidence for 1 nm pores in "dry" thermal SiO_2 from high resolution transmission electron microscopy. *J Electrochem Soc* 127(12):2722.
48. Hasegawa M, et al. (2000) Positron and positronium studies of irradiation-induced defects and microvoids in vitreous metamict silica. *Nucl Instrum Methods Phys Res B* 166:431–439.
49. Yin L, et al. (2015) Mechanisms for hydrolysis of silicon nanomembranes as used in bioresorbable electronics. *Adv Mater* 27(11):1857–1864.
50. Ito T, et al. (1982) Advantages of thermal nitride and nitroxide gate films in VLSI process. *IEEE J Solid-State Circuits* 17(2):128–132.
51. Balk P, Eldridge JM (1969) Phosphosilicate glass stabilization of FET devices. *Proc IEEE* 57(9):1558–1563.
52. Min Yan M, et al. (2005) A transparent, high barrier, and high heat substrate for organic electronics. *Proc IEEE* 93(8):1468–1477.